

Rotor Blade Airfoil Design for High-Altitude, Long-Endurance VTOL UAVs

Preston B. Martin*

Army / NASA Rotorcraft Division

Aeroflightdynamics Directorate, AMRDEC

US Army Research, Development, and Engineering Command

Ames Research Center, Moffett Field, CA 94035

The problem of minimizing blade profile power for a conceptual high-altitude UAV compound helicopter was addressed through airfoil design. Some example performance calculations were presented for a generic configuration at altitudes ranging from 5,000 *ft* to 60,000 *ft*. These performance estimates helped to define the design requirements for high-altitude rotor blade airfoils. Results showed that the combination of natural laminar flow with improved transonic characteristics could enable cruise altitudes up to 50,000 *ft*. The results also showed that for optimum endurance the rotor tip Mach number had to be increased with altitude. The objective of the design effort was the development of transonic, natural laminar flow airfoils for cruise at 50,000 *ft*. The aerodynamic challenges involved the combination of high-subsonic Mach numbers with low Reynolds numbers. This combination of parameters resulted in the appearance of both shock waves and laminar separation bubbles in the relevant flow physics. The design of a highly reflexed inboard airfoil, AFDD 50K30, enabled the use of more camber over outboard sections. This allowed the working section airfoil, AFDD 50K60, to be designed for significant runs of laminar flow. Finally the tip airfoil, AFDD 50K80 was designed for low drag at zero to slightly negative lift found on the advancing blade at high speeds. Results were compared to existing rotorcraft airfoils over the high-altitude design space.

Nomenclature

a_s	Local speed of sound, <i>ft/sec</i>	R	Rotor radius, <i>ft</i>
AR	Wing aspect ratio	S	Wing area, <i>ft</i> ²
b	Wing span, <i>ft</i>	T_{tf}	Thrust of turbofan, <i>lbs</i>
c	Airfoil chord, <i>ft</i>	V_∞	Aircraft forward speed, <i>ft/s</i>
C_d	Airfoil drag coefficient	V_{tip}	Tip speed, <i>ft/sec</i>
C_{d_0}	Airfoil zero lift drag coefficient	W_{to}	Aircraft gross weight at takeoff, <i>lbs</i>
C_{d_w}	Wing airfoil 2D drag coefficient	α	Airfoil angle of attack, <i>deg</i>
C_l	Lift coefficient, rotor blade element	α_{TTP}	Angle of attack of rotor tip path plane, <i>deg</i>
C_L	Lift coefficient, wing	ΔC_{d_c}	Additional drag due to compressibility
C_p	Pressure coefficient	ΔC_{d_l}	Additional drag due to lift
C_{P_t}	Total rotor power coefficient	γ	Ratio of specific heats
C_{P_i}	Rotor induced power coefficient	Λ	Sweep angle, <i>rad</i>
C_{P_o}	Rotor profile power coefficient	λ	Rotor inflow velocity ratio
C_{P_p}	Rotor parasite power coefficient	μ	Rotor advance ratio, V_{tip}/V_∞
C_T	Thrust coefficient	ρ	Density, <i>slug/ft</i> ³
D_f	Fuselage drag, <i>lbs</i>	σ	Rotor solidity, $N_b c / (\pi R)$
D_w	Wing drag, <i>lbs</i>		
D_r	Rotor drag, <i>lbs</i>		
D_t	Total aircraft drag		
e	Wing span efficiency factor		
FM	Total system figure of merit, $C_T^{3/2} / (\sqrt{2} C_P)$		
f_e	Effective flat plate area of fuselage, <i>ft</i> ²		
L_w	Total wing lift, <i>lbs</i>		
M	Local airfoil Mach number		
M_{dd}	Drag divergence Mach number		
M_{90}	Advancing blade Mach number		
N_b	Number of blades		
P_{alt}	Freestream static pressure at altitude, <i>lbs/ft</i> ²		
q	Freestream dynamic pressure, <i>lbs/ft</i> ²		
Re	Reynolds number based on chord length		

Introduction

The challenges of airfoil design for high-altitude aircraft have been researched by the developers of fixed-wing UAVs for atmospheric sampling missions, weapons platforms, ballistic missile defense, and military reconnaissance. The primary reason for using a UAV in place of a piloted aircraft is that the weight of a pilot and life support equipment typically exceeds the payload requirement of the high-altitude mission (Ref. 1). One of the first efforts was a long endurance, high-altitude airfoil targeted for an 82 *ft* wing span 1100 *lb* UAV at 66,000 *ft* (Ref. 2). The 20,000 mile range and 90 hour endurance requirements demanded a new approach to the airfoil design process tailored to the operational requirements. The result was the development of the NASA NLF(1)-1015 airfoil which was an improvement from the classical Wortmann FX63-137 over the design lift coefficients. One characteristic

*Research Scientist

31st European Rotorcraft Forum, Sept. 13–15, 2005 Florence, Italy. For permission to copy or republish, contact the US Army Aeroflightdynamics Directorate Ames Research Center, Moffett Field, CA

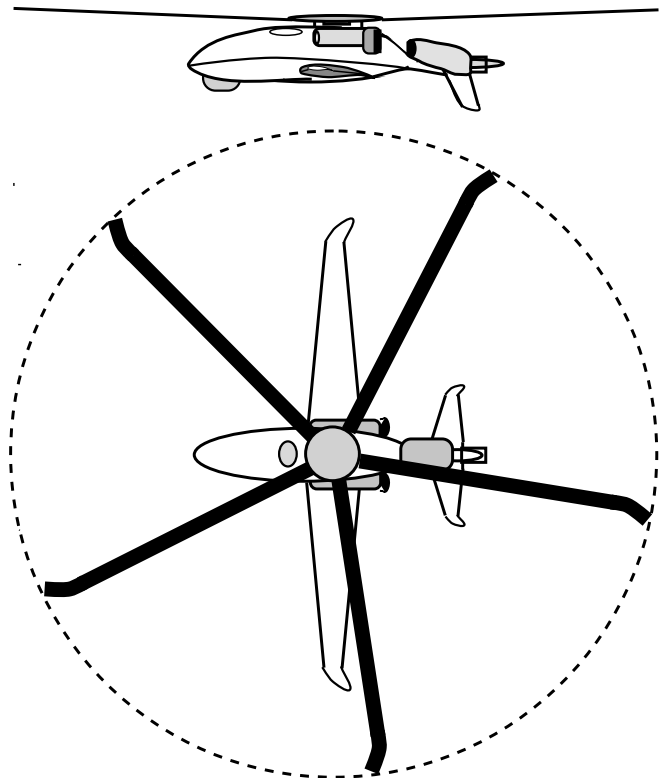
of both of these airfoils is that the maximum lift is not reduced by leading edge roughness; however, the low lift performance is degraded with roughness. At low angles of attack, these airfoils suffer from a sharp drag rise due to separation in the cove created by the aft loaded camber distribution. For this reason, the use of such an airfoil on a rotor blade would incur a significant penalty on the advancing blade. Even so, the procedure to custom tailor an airfoil to specific multi-point design requirements as outlined by Ref. 2 presents an example that will be followed in the current work. Another benchmark from this design study was the realization that high lift could be obtained at low Reynolds numbers, and in fact, the low Reynolds number could be exploited to sustain 50% laminar flow on both sides of the airfoil in order to reduce drag.

While the development of the NLF(1)-1015 airfoil was focused on low Reynolds number performance, another study combined the additional problem of high subsonic Mach numbers encountered at high-altitude (Ref. 3). The resulting transonic flow was found to severely impact the design at high-lift with the formation of lambda shock structures in proximity to laminar separation bubbles. In this design study, the validation of the MSES code was found to be in good agreement with the sparse amount of data representative of these flight conditions. The study was focused on altitudes in excess of 100,000 *ft* requiring lift coefficients of $C_l = 1.3$ at $M = 0.6$ and $Re = 200,000$. Again, the use of an aft loaded camber distribution enabled the point design requirement to be met; however, the drag penalty at low angles of attack became more severe with increasing altitude (see Fig. 16 of Ref. 3). While this is less of a problem for a fixed-wing UAV, it presents a significant design challenge to prevent large profile power losses on the advancing blade of a rotor (Ref. 4). The same low angle of attack penalty of aft loading can also be found in Fig. 17 of another study (Ref. 5), where the useable lift coefficient range of the airfoil became nearly a point design at 70,000 *ft* altitude. Both of these studies illustrated the utility of the MSES airfoil design code for point designs, although the code includes a multi-point design capability.

The present airfoil design study attempted to apply the philosophy of the Eppler-style multi-point design method of Ref. 2 using the transonic, low Reynolds number capability of MSES demonstrated by Ref. 3. The objectives of the design were to investigate the challenges of high-altitude rotor airfoils and the multi-point optimization issues related to achieving a global maximum – as pointed out by (Ref. 6). The paper was divided into two parts. In the first part, a representative configuration for a compound helicopter was developed, and a performance study was conducted to determine the flight envelope. The study was repeated using turbulent airfoils, natural laminar flow (NLF) airfoils, and supercritical NLF airfoils. The second part of the paper used the results of the performance study to design three new airfoils for a 50,000 *ft* cruise condition.

Model Problem for a High-altitude, Long Endurance VTOL UAV

The accurate prediction of the periodic airfoil environment at each radial station requires a detailed comprehensive aeromechanics analysis. This must include the induced angles of attack from blade dynamics and aeroelastic response,



Wt = 6000 lb (empty weight = 4000lb)
 3 x RR 250-c20W Turboshaft : 1950 HP total
 1 x Williams/Rolls FJ44-1A Turbofan: 1900 lbs
 Fuel = 1500 lbs
 Payload = 500 lbs

Rotor:
 R = 30ft
 Nb = 5
 solidity = 0.074
 Anti-torque: turbofan thrust vectoring

Wing:
 b = 40ft
 S = 143 ft²
 AR = 12

Fig. 1 High-altitude VTOL UAV concept used for rotor airfoil aerodynamics study.

vortex wake flow physics, fuselage/engine/wing inflow distortion, and trimmed flight control inputs. Many of these details are configuration dependent. There is a balance required in preliminary design between the level of detail and the efficiency of the process. This is especially true when the focus of the effort is on overcoming complex flow physics problems through airfoil design.

Approach

In the present study, a new class of helicopter is under study over a wide range of flight conditions (i.e., altitudes from 5,000 ft to 60,000 ft) and over a wide range of rotor operating conditions. At a minimum, an example baseline study required 2040 cases to be studied to determine the flight enve-

lope, and clearly this precluded a full comprehensive analysis from providing rapid feedback into the airfoil design process. Instead, the current study attempted to reduce the matrix using a more efficient first principles based analysis. As much as possible, the key issues that defined the airfoil environment were included in the analysis. This included simple models of the effects of non-uniform inflow, control inputs, elastic torsional motion, and blade flapping response. The justification for this approach is that it provided a good first approximation to the airfoil environment, and identified the role of airfoil performance in the capabilities of an entirely new class of helicopter. In addition, the efficiency of the method allowed an airfoil design code, a transonic airfoil analysis code, and an airfoil optimization code to be coupled together and linked to the rotorcraft performance code. The approach was by no means a substitution for proper comprehensive analysis, and the results must be verified and refined in a follow-on effort over a small subset of the flight envelope. This would occur once more details of a specific design or configuration are developed.

Configuration

In order to begin to define the airfoil environment, some details of a specific configuration were required. The high-altitude, long endurance VTOL UAV concept used in this study is shown in Fig. 1. The initial sizing of the aircraft was based on the requirement for maximum endurance carrying a 500 lb payload over a range of altitudes from 30,000 ft to 50,000 ft with a service ceiling of 60,000 ft. The configuration of a compound helicopter with auxiliary thrust was chosen as a good candidate for the high altitude requirement. The maximum wing span was limited to 2/3 of the rotor diameter in order to avoid blade strikes during ground run-up in adverse winds. A low wing design was required for the same reason. The planform of the wing was based on a high-altitude design lift coefficient of 1.5 balanced with the requirement for minimum download in hover. The low disk loading of the rotor (2 *psf* in hover) provides for excellent hover efficiency.

Preliminary engine selection was based on currently available models with technology advancement factors assumed for the high-altitude performance. The number of turboshaft engines was allowed to change between two and three, but a single turbofan was assumed to keep installation drag to a minimum. The models chosen were characterized by their compact size and minimum weight. The turboshaft engines are found on other VTOL UAVs such as the Firescout, and the turbofan engine is similar to that used on a jet version of the Predator fixed-wing UAV. In addition to minimizing signature, the placement of the turbofan inlet downstream of the rotor pylon fairing is conceptually for the purpose of reducing hub/pylon drag. The inlet design for such a concept is not trivial, since a variable guidevane system and variable pitch compressor blades would be required in order to avoid flow distortion losses and unsteadiness. In hover and at low speeds where the downward V-tail is ineffective, a turbofan thrust vectoring system is proposed for anti-torque. In this case, the inlet location minimizes particle ingestion into the turbofan as much as possible. The drag of the fuselage assumes significant amounts of laminar flow and no separation through a

combination of design and flow control. The minimum obtainable effective flat plate area of the fuselage without the wing was assumed to be 5 ft^2 .

The concept used for this study is purely theoretical and has no relationship to any current government program or US Army acquisition plans. The concept was developed for research purposes in order to study the airfoil design aspects of this class of UAV.

Performance Analysis Method

The analysis method used empirically corrected performance equations for the rotor combined with simple finite wing aerodynamic theory. Once a trim state was determined, the blade element environment was calculated with a modified form of the Beddoes prescribed wake method (Ref. 7) coupled with simple models of blade flapping and torsional motion (Ref. 8). Engine sea level specifications were found from manufacturer data, but theoretical lapse rates (with technology improvement factors of 20%) were used for performance estimates at altitude.

Design Profile Drag Estimate

The fundamental barrier to high-altitude UAV rotor performance is the rapid rise in profile power due to shock boundary layer interactions at high lift. A zero order model of the drag increments is presented in order to begin to define the high altitude airfoil design requirements.

The advancing tip Mach number (accounting for a swept tip) is

$$M_{90} = \left(\frac{V_{tip}}{a_s} \right) (1 + \mu) \cos(\Lambda_{tip}) \quad (1)$$

and the airfoil drag divergence Mach number is assumed to be a function of the blade loading (Ref. 9)

$$M_{dd} = 0.95 - 2.5 \frac{C_T}{\sigma} \quad (2)$$

The effect of high performance transonic airfoils was idealized by using $C_T = 0$ in the above equation. When the advancing tip Mach number had exceeded the drag divergence value then a compressibility correction (Ref. 9) is added to the average sectional drag coefficient

$$\Delta C_{dc} = 0.2 (M_{90} - M_{dd})^3 + 0.0085 (M_{90} - M_{dd}) \quad (3)$$

In addition, the increase in drag with lift was estimated by adding the following function of blade loading to the sectional drag coefficient (Ref. 8)

$$\Delta C_{d_l} = \frac{9C_{d_o} \left(1 + \frac{8\mu^2}{9} \right)}{4\sigma\mu} C_T^2 \quad (4)$$

where the same correction was always applied for all of the classes of airfoils. The total sectional drag coefficient is then estimated to be

$$C_d = C_{d_o} + \Delta C_{dc} + \Delta C_{d_l} \quad (5)$$

where the minimum drag for natural laminar flow airfoils was idealized as $C_{d_o} = 0.006$ and the minimum drag of conventional fully turbulent flow airfoils was $C_{d_o} = 0.010$. This first

order estimate of profile drag was used to help define the target for airfoil design and to determine the influence of airfoil design on the flight envelope.

The purpose of this study was to design a series of airfoils where the first two terms of Eq. 5 are minimized at high-altitude. As will be shown, it is the rapid rise in profile power that limits the ceiling of low disk loading high-altitude rotors. It is anticipated that if the airfoil design problem is solved, then a new class of helicopter will become increasingly competitive with fixed wing high-altitude UAVs – with the added advantage of vertical takeoff and hover capability at lower altitudes.

Power Curve Estimate

The total power coefficient, C_{P_t} , is estimated as a function of induced power from Ref. 8,

$$C_{P_i} = 1.075 \cosh(7.5\mu^2) \frac{C_T^2}{2\sqrt{\mu^2 + \lambda^2}} \quad (6)$$

and profile power,

$$C_{P_o} = \frac{\sigma C_d}{8} (1 + 4.65\mu^2 + 4.15\mu^4 - \mu^6) \quad (7)$$

where the total drag coefficient including corrections for compressibility and lift was used in place of C_{d_o} in this equation from Ref. 8.

The parasite power was,

$$C_{P_p} = \frac{1}{2} \left(\frac{f_e + C_{D_w} S}{A} \right) \mu^3 \quad (8)$$

where the total effective flat plate area, f_e , is equal to the sum of contributions from the fuselage, hub, tail, etc, and a contribution from the total wing drag, $C_{D_w} S$. Rotor/wing interference drag was ignored, but this assumption is only valid for a low wing in cruise. Normally, the total rotor power required would include this parasite term, but in this study auxiliary propulsion from a turboprop was assumed to provide the required thrust. The tip-path-plane angle of attack was assumed to be zero, with cyclic controls applied to zero out harmonic flapping. As a result, the total shaft power required by the rotor was

$$C_{P_t} = C_{P_i} + C_{P_o} \quad (9)$$

Trim State

The total thrust required from the turboprop was equal to the total drag

$$T_{tf} = D_t \quad (10)$$

where the total drag was a sum of contributions from the wing, rotor, and fuselage

$$D_t = D_w + D_r + D_f \quad (11)$$

The total wing drag was estimated using

$$D_w = \left(\frac{C_L^2}{e\pi AR} + C_{d_w} \right) qS \quad (12)$$

The effective drag of the rotor was approximated by

$$D_r = \frac{C_{P_i} \rho_{alt} A V_{tip}^3}{V_\infty} \quad (13)$$

and this approach is obviously over conservative. The parasite drag of the fuselage was

$$D_f = qf_e \quad (14)$$

The total thrust required from the rotor was equal to the aircraft weight minus the wing lift.

$$T = W_{to} - L_w \quad (15)$$

and no variation over time with fuel burn was used. For this simple study, the wing was assumed to be operating at a high lift-to-drag ratio, and the lift coefficient was prescribed as a constant $C_L = 1.5$. This is representative of high-altitude, fixed-wing UAVs, and allows the analysis to assume an optimized, high-performance wing. The lift on the wing varied with forward speed $V_\infty = \mu V_{tip}$ and altitude according to

$$L_w = \frac{1}{2} \rho_{alt} (\mu V_{tip})^2 C_L S \quad (16)$$

where the density at a given altitude ρ_{alt} was found by assuming a standard atmosphere. The ratio of rotor thrust to wing lift can be written as three terms corresponding to the wing, the ambient conditions at altitude, and the rotor

$$\frac{T}{L_w} = \left(\frac{2W_{to}}{C_L S} \right) \left(\frac{1}{\gamma P_{alt}} \right) \left(\frac{1}{(\mu M_{tip})^2} \right) - 1 \quad (17)$$

This study assumed the first term to be constant, varied the second term by changing altitude, P_{alt} , and varied the third term by changing both the rotor tip Mach number M_{tip} and the advance ratio μ . This form of the equation illustrates the increase in the ratio of T/L_w as altitude increases (i.e., pressure decreases).

Blade Element Analysis

Using the results of the integrated performance study, a blade element analysis was performed at the cruise condition for 50,000 ft. The classical blade element equations used in the study were from Ref. 7, and will not be repeated here; however, a few additional details were included in the definition of the effective angle of attack at each blade section.

A modified version of the Beddoes prescribed wake (Ref. 7) was developed. The unique feature of the Beddoes model is that the vertical displacement of the tip vortices is determined from the integrated effect of an assumed inflow distribution. Instead of using the semi-empirical inflow equation developed by Beddoes, the vertical displacement of the tip vortices was integrated using the Mangler and Squire inflow model (Ref. 7). The added advantage of this approach is that it captures the effects of highly nonuniform inflow near the edges on vertical wake spacing, without resorting to a full free wake analysis. This appeared to be very important for predicting the vortex induced angles of attack when the rotor was operated at zero tilt of the tip-path-plane.

The induced angles of attack from blade motion were estimated using a simple theory (Beavan and Lock) for blade torsion from Ref. 8 and the assumption of harmonic flap motion. The control settings were determined by requiring zero lateral and longitudinal flapping. A precone of 2° was also assumed. One important note about the blade motion is that the Lock number is reduced by a factor of approximately

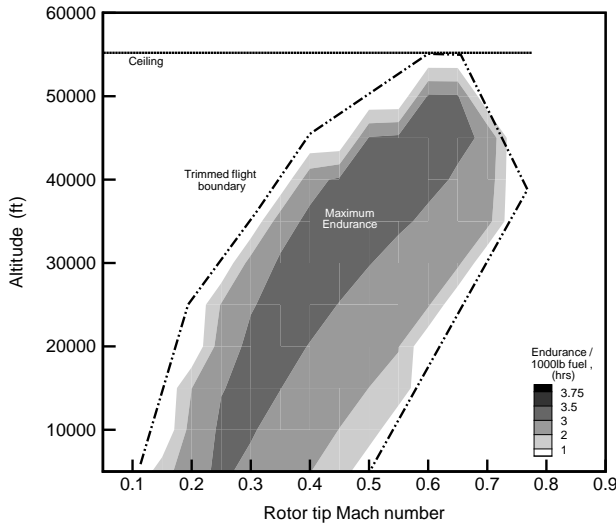


Fig. 2 Cruise endurance for $W_t = 6000$ lb, using turbulent flow airfoils.

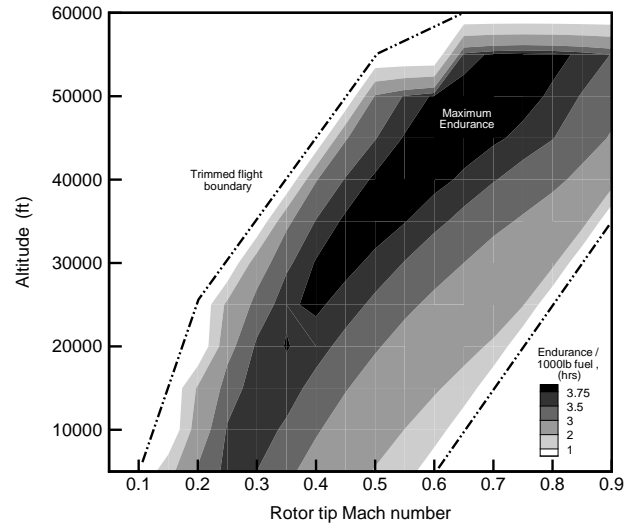


Fig. 4 Cruise endurance for $W_t = 6000$ lb, using laminar flow airfoils with improved M_{dd} .

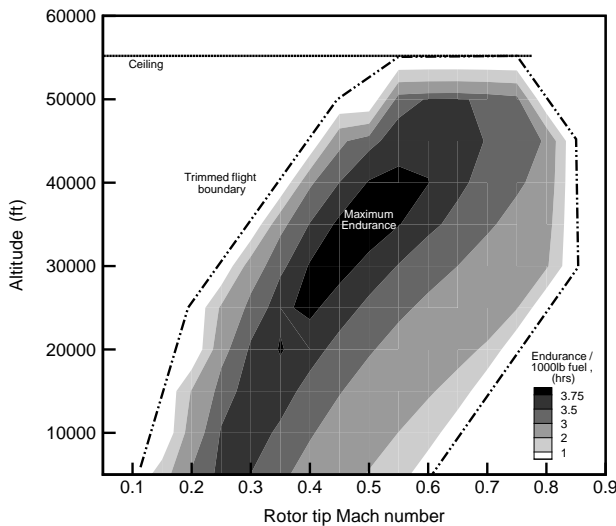


Fig. 3 Cruise endurance for $W_t = 6000$ lb, using laminar flow airfoils.

ten at high-altitude. This results in a condition of small flap damping and reduced torsional sensitivity to non-zero airfoil pitching moment. More detailed studies are required from full comprehensive analysis to better understand the blade dynamics at low air density conditions.

High-Altitude Performance Study

The composite results of the performance calculations over the entire flight envelope are shown in Figs. 2 to 4. In each of these figures, the endurance during the cruise portion of the flight profile (assuming a 1000 lb fuel burn) is plotted as a function of the rotor's hover tip Mach number and the aircraft's pressure altitude. Endurance was selected as the quantity of interest, because the most likely role of high-altitude UAVs is reconnaissance. The maximum endurance was cal-

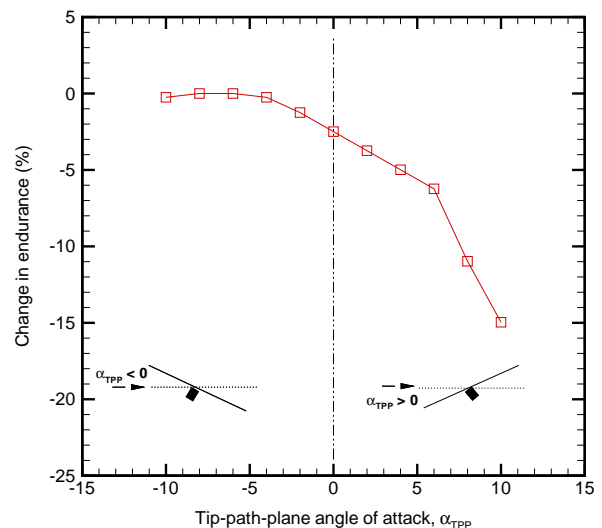


Fig. 5 Change in maximum endurance with angle of attack of the tip-path-plane, α_{TPP} .

culated by performing a forward speed sweep (varying μ) at each combination of tip Mach number M_{tip} and altitude. Each combination uniquely determined the ratio of rotor thrust to wing lift according to Eq. 17. Rotor tip Mach number was used instead of rotor tip speed or angular velocity, so that the results were plotted independent of the decrease in sonic velocity with altitude. The weight was also assumed constant during the cruise, and so the absolute numbers for endurance are conservative. In this study, the absolute values for cruise endurance during a 1000 lb fuel burn are not as important as the values relative to the baseline.

The purpose of this study was to: (1) help better understand the optimum load sharing between the wing and the rotor at high altitude from integrated performance results, (2) deter-

mine the sensitivity of high altitude performance to advanced airfoil design, (3) estimate the aerodynamic environment and define the airfoil design objectives.

Integrated Performance

There are many concepts of slowed-rotor compounds, where the rotor is slowed in forward flight and completely unloaded. This is possible and efficient at lower altitudes because of the high dynamic pressure available to the wing. At an altitude of 60,000 ft, however, the air density drops to approximately 10% of the sea level value. As a result, a slowed rotor compound design would require ten-times the wing area for the same load sharing between the wing and rotor. For the assumed wing design in this study, the results show that optimum endurance requires the rotor speed to be increased with increasing altitude. One obvious question related to whether or not tilting the rotor back into autogyro mode would be beneficial. The relative change in maximum endurance is shown in Fig 5 as a function of rotor angle of attack. There appears to be very little improvement since the high-altitude rotor is already at an advance ratio for minimum induced drag, and the small power savings is offset by increased fuel consumption of the turbofan to overcome the additional rotor drag. A more detailed study should include the effect of operating in this mode on the aerodynamic environment. It appears from Ref. 10 that the radial lift distribution of an autogyro changes as would be expected. The slightly increased angles of attack near the tip would cause earlier shock formation, and the high inboard angles of attack would cause stall because of the low Reynolds number. For these reasons, the current study was conducted at zero angle of attack of the tip-path-plane with zero cyclic flapping (and a finite coning angle).

The trimmed flight envelope is also shown as a dashed line surrounding the contours of endurance. The boundary to the left (Figs. 2 to 4), at lower tip Mach number, was primarily from an increase in rotor drag (H-force) that exceeded the thrust available from the turbofan. This increase in rotor drag was caused by the reduced tip speed forcing the rotor to operate at high blade loading with corresponding high profile drag. The boundary to the right, at higher tip Mach number, occurred when the required rotor power exceeded the available turboshaft power. At lower altitude this occurred when the increased tip speed caused the advance ratio to decrease, forcing a rise in rotor induced power. At higher altitudes, both boundaries were a function of the compressible flow, profile power rise, and so they joined to form the absolute ceiling.

Performance Sensitivity to Airfoil Design

As a result, the high-altitude performance and ceiling were a strong function of the rotor airfoil performance. Fig. 2 assumed a typical value of $C_{d_o} = 0.01$ for fully turbulent airfoils with a standard drag rise with increased lift (Eq. 4) and Mach number (Eq. 3). The performance at the design altitude of 50,000 ft is poor, and the ceiling is approximately 55,000 ft. Fig. 3 assumed a typical value of $C_{d_o} = 0.006$ for advanced natural laminar flow (NLF) airfoils using a standard drag rise with lift and Mach number. The maximum endurance was increased dramatically, and an optimum in cruise altitude appeared from 30,000 ft to 40,000 ft, i.e., once the rotor power was minimized, the performance became a function of the turbofan specific fuel consumption. Despite these improve-

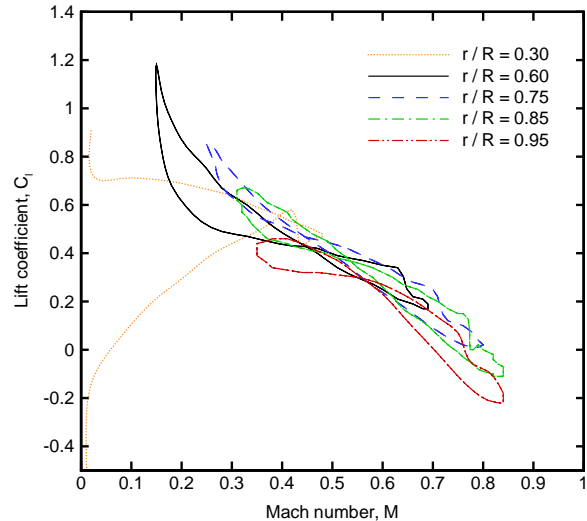


Fig. 6 Airfoil environment with $\theta_{tw} = -8^\circ$, Altitude = 50,000 ft, $\mu = 0.39$, $C_T/\sigma = 0.08$, $V_\infty = 150$ kts, $T/W = 0.5$, $M_{tip} = 0.7$, $M_{1,90} = 0.84$.

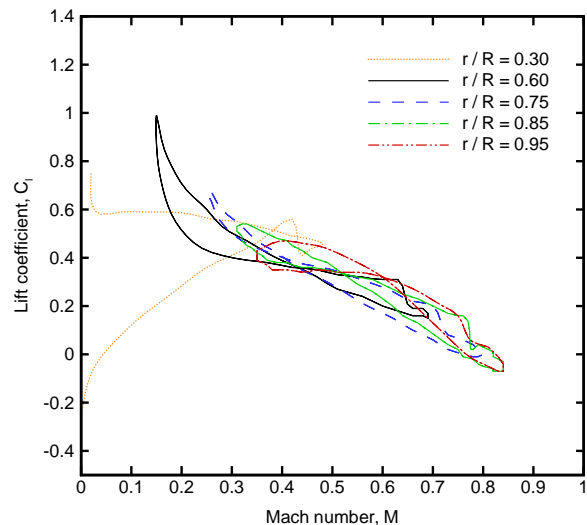


Fig. 7 Airfoil environment with optimized twist, Altitude = 50,000 ft, $\mu = 0.39$, $C_T/\sigma = 0.08$, $V_\infty = 150$ kts, $T/W = 0.5$, $M_{tip} = 0.7$, $M_{1,90} = 0.84$.

ments, the ceiling was not changed by the use of NLF airfoils.

In Fig. 4, the compressible drag rise characteristics of the NLF airfoils were assumed to be improved from the standard model (Eq.3). This improvement resulted in both increased endurance and increased ceiling, as well as optimized performance over a range of altitudes of 30,000 ft to 55,000 ft - meeting the original design goals.

The use of NLF airfoils on rotorcraft has often been precluded by operational environments at low altitudes where leading edge contamination occurs due to dust, sand, water, insects, and blade erosion. The idea of using natural laminar flow airfoils on a high-altitude helicopter assumes; first,

that a high rate of climb at sea level will be available to minimize leading edge exposure, and second, that the rotor blades would be maintained according to the science/art of laminar flow. Another factor that might influence how much natural laminar flow is possible is the effective turbulence level of the rotor environment. The ultimate success of this concept can only be determined by extensive testing, and so the current study only aims at building support for more research into this area.

Design Objectives

The study used a description of a class of airfoil by using a model for the drag. The result was useful for design purposes because it identified the characteristics of the airfoil that had the most impact on high-altitude performance. In this case, it appeared that not only could natural laminar flow dramatically increase endurance, but also careful attention to compressible drag rise could increase service ceiling. All of the results also assumed attached flow with no drag rise due to stall.

Two cases for the blade element / prescribed wake aerodynamic environment are shown in Figs 6 and 7. Parabolic sweep was assumed for both cases in order to maintain a tip with constant Mach number as function of radius. During the initial development of the starting airfoils, the twist was assumed to be linear, see Fig. 6. A typical helicopter rotor blade would have more twist, but an attempt was made to minimize the amount of negative lift at the tip in forward flight. Figure 6 shows the predicted variation of airfoil lift coefficient with Mach number over one rotor revolution. The rotor was lightly loaded, and the advance ratio was low enough to avoid retreating blade stall. The signature of the vortex induced angle of attack change was observed on the advancing blade. Under light loading with no shaft tilt, the vortex wake remained close to the tip-path-plane.

Near the tip, the advancing blade suffered from negative lift coefficients shown in Fig. 6. Preliminary results showed this combination of negative lift coefficient with high subsonic Mach number resulted in shock boundary layer interaction on the lower surface of the leading edge. This made the design of for natural laminar flow nearly impossible. For this reason, the twist was optimized to reduce the magnitude of the negative lift on the advancing tip. The airfoil environment for this case is shown in Fig. 7. An added benefit was that the retreating blade maximum lift was reduced. The results in Fig. 7 were used as the target airfoil design points. The objective was to design natural laminar flow airfoils that performed with advancing blade drag coefficients of $C_d = 0.006$ or less.

Airfoil Design Tool

The conformal mapping approach of the Eppler code (Ref. 11) was the primary airfoil design tool used in this study to develop good starting airfoils for the multi-point optimization process. The design was specified in the transformed complex plane, where the airfoil is represented by a circle. Once a design was generated, the result was analyzed using MSES at ten blade azimuths in order to check the transonic and low Reynolds number performance. The process was repeated to minimize the adverse flow physics associated with

laminar separation bubbles and shock waves. In most cases, the starting airfoil was very close to optimum.

Using results of the rotor performance code, a multipoint optimization problem was generated and used the geometry output of the Eppler code as an initial condition. The primary tool for the final optimization study was MSES and its subprogram LINDOP. This numerical analysis uses an Euler solution on a streamline based inviscid grid, and an integral boundary layer solution near the wall. The Euler and viscous solutions are coupled using the displacement thickness and solved with a global Newton method (Ref. 12). This allows both inverse and direct solution/design capability. Details of the code are presented in (Ref. 13).

Design Results

The requirement of high-lift at high, subsonic Mach number combined with low Reynolds number places severe challenges on the airfoil design. These challenges are similar to those faced by designers of high-altitude fixed-wing UAVs, Refs. 2 and 3. Three new airfoils were designed for the root, working section, and tip of a conceptual rotor. The final airfoil coordinates are shown in Figs. 8 to 10.

AFDD 50K30 Airfoil, $r/R = 0.30$

The design of the inboard blade section was primarily driven by the requirement for a high, positive pitching moment used to offset the use of aft loaded airfoils outboard. As shown by Ref. 14, the absolute value of the inboard reflexed airfoil pitching moment must be two-times that of the aft loaded section. Such a high positive pitching moment is outside the abilities of a simple tab. The use of a highly reflexed camber line requires the portion of the airfoil forward of the quarter chord to generate positive lift. The amount of lift must compensate for the negative lift generated by the aft portion of the airfoil.

The combination of low Reynolds number and high subsonic Mach number caused a severe design challenge near the leading edge for the advancing blade design point, and on the lower surface of the trailing edge for the retreating blade design point. As shown by Fig. 11, the formation of a laminar separation bubble occurred at the same location on the leading edge where a pocket of supersonic flow created a shock on top of the bubble. The result was an unhealthy turbulent boundary layer that re-separated before reaching the 3/4 chord station. The retreating blade Reynolds number was 210,000, and the flow shown in Fig.12 was dominated by laminar separation bubbles on both the upper and lower surface. On the the lower surface, the bubble did not re-attach and there was a significant pressure drag penalty. These flow physics proved to be outside of the capabilities of the optimizer to fix, and so the airfoil was redesigned using a traditional approach.

The result is shown in Figs. 13 and 14, where the advancing blade design point no longer suffered from separated flow, and the lower-side bubble of the retreating blade design point was forced to reattach. The drag was reduced by 50% for the advancing blade design point, and by 30% for the retreating blade design point; however, the pitching moment had to be decreased. It is interesting to note that the resulting airfoil is similar to one of the first NACA helicopter sections, the

NACA 6H10.

AFDD 50K60 Airfoil, $r/R = 0.60$

Using results from the rotor analysis, the design space for the 60% radial station is shown in Fig. 15 where the Mach number ranges from 0.15 to 0.70, and the Reynolds number ranged from 150,000 to 1.1 million. Using these conditions a starting airfoil was generated, and the Mach number distribution is shown in Fig. 16 for the advancing blade design point. The airfoil was designed to maintain subsonic flow, and a significant run of laminar flow. The advancing blade drag was $C_d = 0.0070$. Next, the starting airfoil was run through a ten-point design optimization using LINDOP, subject to the constraints on lift coefficient. The objective function was the sum of the drag values at each of the design points. The airfoil shape was modified using a series of mode shapes based on Chebyshev polynomials. After a few steps, the leading edge was changed, and the drag was reduced to $C_d = 0.0060$, but some high frequency surface waviness was a by-product of the optimizer, see Fig. 17. As a result, the airfoil was smoothed using inverse design by specifying a smoothed pressure distribution, and solving for the airfoil geometry. During this step, a finite trailing edge thickness was added to ease manufacturing difficulties. The change in airfoil shape is shown in Fig. 18, and the resulting velocity distribution is shown in Fig. 19. As a result of the finite trailing edge thickness, the drag increased slightly to $C_d = .0062$. Such a low value of drag is the benefit of designing for laminar flow.

For comparison, the same advancing blade design point for the VR12 assuming free transition is shown in Fig. 20. The transition point occurs near 30% on the upper surface and at 4% on the lower surface, so the airfoil boundary layer is mostly turbulent. As a result, the drag coefficient, even with the assumption of free transition, is $C_d = 0.01$. The reason for the higher drag is that the flow formed a supersonic pocket terminating with a small shock that did not form on the AFDD 50K80 airfoil, see Fig. 21 compared to Fig. 22. The interaction of this shock with the boundary layer increased the boundary layer thickness on the lower side of the VR12 airfoil, see dotted line in Fig. 22.

The performance of the initial AFDD 50K60 at the retreating blade design point is shown in Fig. 23 compared to both the final airfoil Fig. 24 and the VR12 (Fig. 25). The retreating blade flow physics were dominated by the formation of a laminar separation bubble on the upper surface leading edge and on the lower surface of the trailing edge. The reason for the formation of the bubble is that the Reynolds number is not high enough for transition to occur before the boundary layer undergoes laminar separation. After separating, transition is triggered in the detached shear layer, and the flow re-attaches as a turbulent boundary layer. On the VR12, this turbulent boundary layer then re-separates before reaching the trailing edge (see Fig. 25). After optimization, the final version of the airfoil shown in Fig. 24 overcomes this problem, and the drag polar shown in Fig. 26 is improved over the entire range of design C_l .

AFDD 50K80 Airfoil, $r/R = 0.80$

As shown by the rotor analysis in Fig. 6, the use of nonlinear twist and parabolic sweep creates a similar aerodynamic

environment for the outer 20% of the blade radius. Using the same procedure described in the previous section, the tip airfoil was designed for low drag. The starting airfoil is shown in Fig. 27 for the advancing blade conditions, and in Fig. 28 for the retreating blade conditions. The final results are shown in Figs. 29 and 30 for the initial airfoil, the final AFDD 50K80 airfoil, and the SSC-A09. The AFDD 50K80 airfoil was designed for very low drag by using laminar flow over 70% of both surfaces at subcritical Mach numbers. The drag bucket (see Fig. 30) was moved to negative lift commonly found on high speed advancing tips. For the advancing blade condition (Figs. 32 and 31), the flow becomes supersonic, and so the design attempts to minimize the shock strength. As shown by Fig. 34, strong shocks form on both sides of the SSC-A09 airfoil, and the lower drag of the AFDD 50K80 is achieved in part by minimizing these shocks. The performance at high lift was traded for the low drag at near zero lift.

Conclusions

1. The influence of rotor airfoil design on high-altitude compound helicopter performance was estimated using a simple first principles approach. The results of the study showed a potentially significant impact of natural laminar flow airfoils on the cruise endurance at 50,000 *ft*. Maximum endurance was obtained at high-altitude by increasing the rotor tip Mach number, because the wing was operating in very low dynamic pressure. The absolute ceiling of the flight envelope was determined by compressible flow drag rise.
2. The airfoil environment for cruise at 50,000 *ft* posed serious flow physics challenges for the design of natural laminar flow airfoils. Three new airfoils were designed for the root, working section, and tip of a conceptual rotor. The final airfoil coordinates are shown in Figs. 8 to 10.
3. The root airfoil, AFDD 50K30, was designed to provide positive pitching moment used to offset the aft loaded camber of the working section airfoil. Laminar separation bubbles had to be minimized for the retreating blade design condition, and shocks had to be avoided for the advancing blade conditions.
4. The working section airfoil, AFDD 50K60, took advantage of the low Reynolds number environment with over 50% laminar flow. The airfoil drag coefficient for the advancing blade was $C_d = 0.006$, and a lower surface shock was prevented compared to the VR12.
5. The tip airfoil, AFDD 50K80, was designed with 50% to 70% supersonic laminar flow, and the shocks on both sides were minimized compared to the SSC-A09. The zero-lift drag at subcritical Mach numbers was less than $C_{d_0} = 0.004$
6. The use of natural laminar flow airfoils on an operational rotorcraft presents several challenges. It is not clear how much laminar flow would be achieved with higher freestream turbulence levels caused by the rotor wake. The use of laminar flow airfoils on low altitude

helicopters is impractical due to sand, dust, insect debris, and rain. More research is required to understand if a high rate of climb is available to minimize low altitude exposure, how much laminar flow would be achievable at altitudes above 30,000 ft.

- The simple analysis methods used for performance and blade element aerodynamic predictions need to be validated over a few cases using a full comprehensive aeromechanics analysis. Several questions remain related to the 10x reduction in Lock number occurring at altitude.

References

- Bentz, D. J., Mockler, T., Maldonado, Hahn, A., Cyrus, J., Schmitz, P., Harp, J., and King, J., "Propulsion Selection for 85kft Remotely Piloted Atmospheric Science Aircraft," NASA TM 107302, AUVSI 96, Orlando, FL, 1996.
- Maughmer, M. D., and Somers, D. M., "Design and Experimental Results for a High-Altitude, Long-Endurance Airfoil," *Journal of Aircraft* Vol. 26, No. 2, pp. 148-153, 1989.
- Drela, M., "Transonic Low-Reynolds Number Airfoils," *Journal of Aircraft*, Vol. 29, No. 6, 1992, pp. 1106-1113.
- Bousman, W. G., "Airfoil Design and Rotorcraft Performance," AHS Forum 58, Montreal, Canada, June 11-13, 2002.
- Tilman, C. P., and Kasim, B., "Supercritical Airfoil Design for Future High-Altitude Long-Endurance Concepts," *Journal of Aircraft* Vol. 41, No. 1, 2004, pp. 156-164.
- Namgoong, H., Crossley, W. A., and Lyrintzis, A. S., "Global Optimization Issues for Transonic Airfoil Design," 9th AIAA/ISSMO Symposium on Multidisciplinary Analysis and Optimization, Atlanta, GA, Sept. 2002.
- Leishman, J. G., *Principles of Helicopter Aerodynamics* Cambridge University Press, Cambridge, UK, 2000.
- Harris, F. D., "Rotary Wing Aerodynamics- Historical Perspective and Important Issues," "National Specialist's Meeting on Aerodynamics and Aeroacoustics," American Helicopter Society, Feb. 25-27, Phoenix, AZ, 1987.
- Stepniewski, W. Z., and Keys, C. N., *Rotary-Wing Aerodynamics*, Dover Publications, New York, 1984.
- McCormick, B. W., "A Numerical Analysis of Autogyro Performance," AIAA 2002-5950, Biennial International Powered Lift Conference and Exhibit, Nov. 5-7, Williamsburg, VA, 2002.
- Eppler, R., and Somers, D. M., "A Computer Program for the Design and Analysis of Low-Speed Airfoils," NASA TM 80210, 1980.
- Drela, M. and Giles, M. B., "Viscous-Inviscid Analysis of Transonic and Low Reynolds Number Airfoils," *AIAA Journal* Vol. 25, No. 10, pp. 1347-1355, 1987.
- Drela, M., "Newton Solution of Coupled Viscous/Inviscid Multielement Airfoil Flows," AIAA Paper 90-1470, AIAA 21st Fluid Dynamics, Plasma Dynamics, and Lasers Conference, June 1990, Seattle, WA.
- Perry, F. J., "Helicopter Rotor Blade," United States Patent 4427344, Jan 24., 1984.

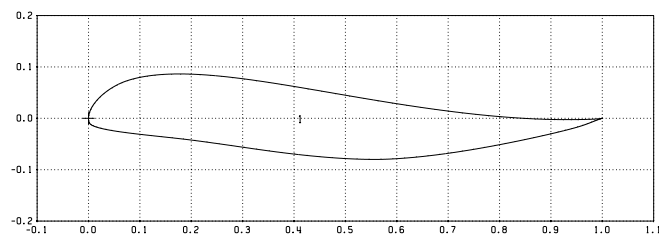


Fig. 8 AFDD 50K30 reflexed airfoil for $r/R = 0.2$ to 0.5 .

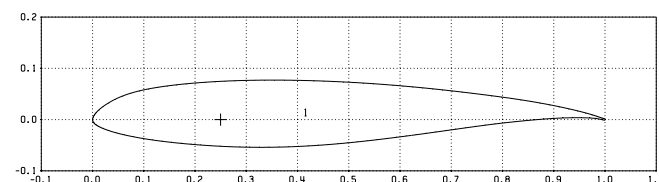


Fig. 9 AFDD 50K60 natural laminar flow airfoil for $r/R = 0.6$ to 0.8 .

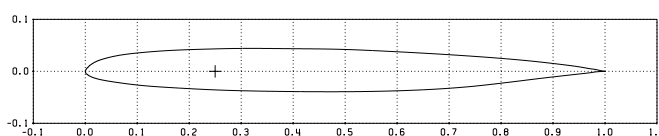


Fig. 10 AFDD 50K80 natural laminar flow tip airfoil for $r/R = 0.8$ to 1.0 .

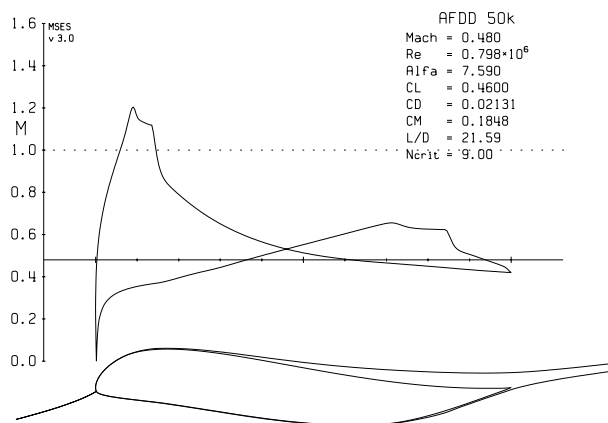


Fig. 11 Advancing blade design point at $r/R = 0.3$, shock induced separation problem.

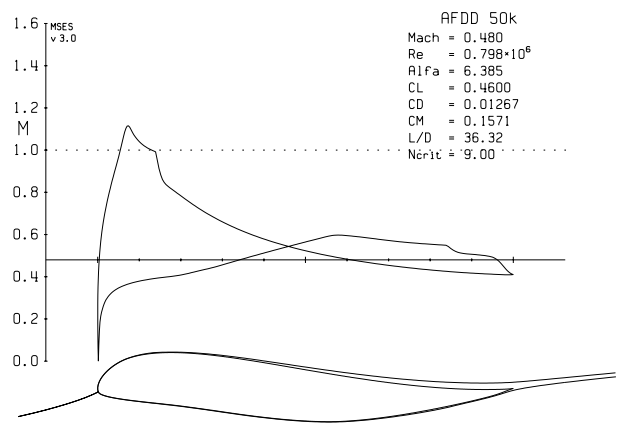


Fig. 13 Advancing blade design point at $r/R = 0.3$, shock induced separation removed.

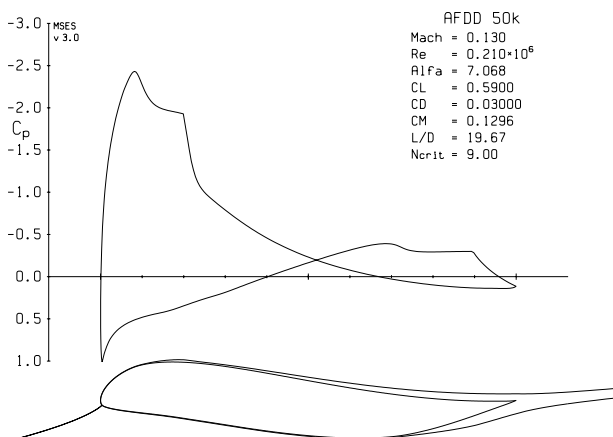


Fig. 12 Retreating blade design point at $r/R = 0.3$, long laminar separation bubble on lower surface.

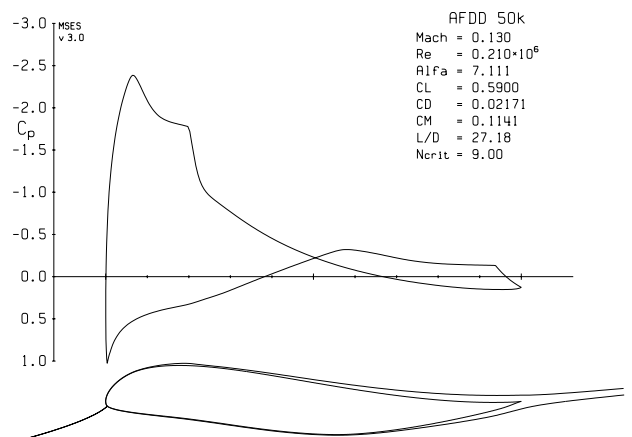


Fig. 14 Retreating blade design point at $r/R = 0.3$, minimized laminar separation bubble on lower surface.

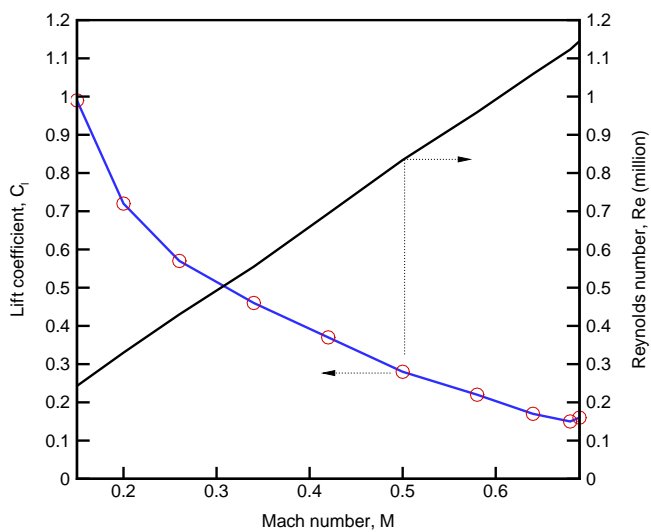


Fig. 15 Design space for $r/R = 0.6$.

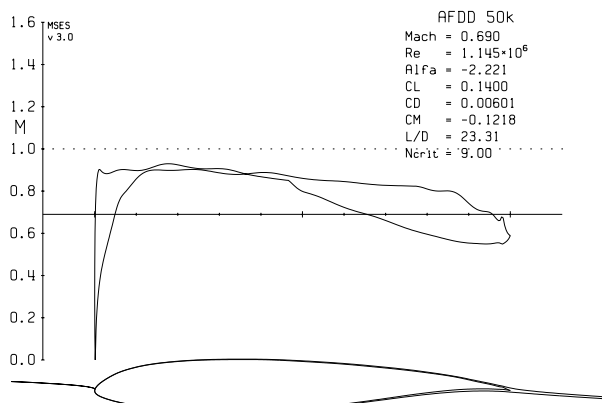


Fig. 17 Design results for advancing blade $r/R = 0.6$ after optimizer, before smoothing.

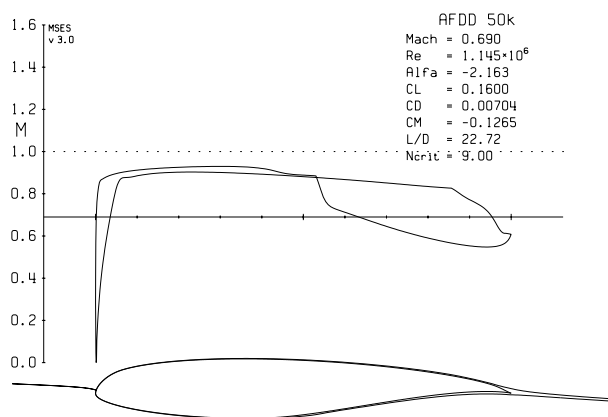


Fig. 16 Design results for advancing blade $r/R = 0.6$ before optimizer.

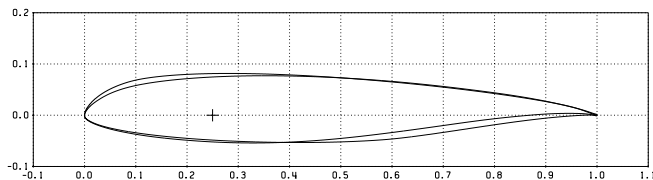


Fig. 18 AFDD 50K60 natural laminar flow, starting and final design.

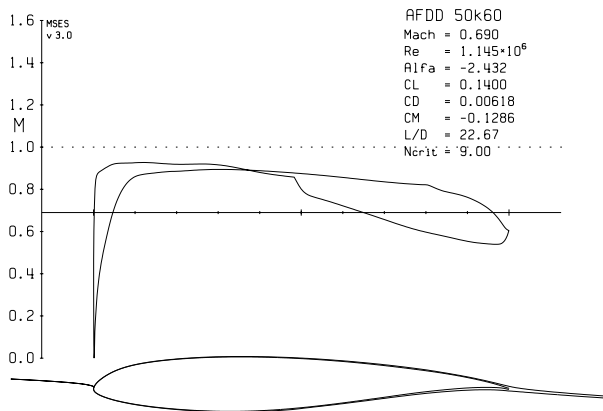


Fig. 19 Design results for advancing blade $r/R = 0.6$ after optimizer, after smoothing.

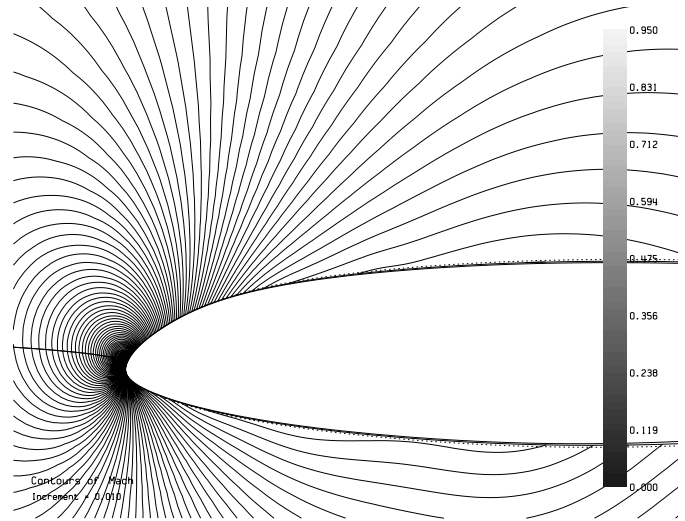


Fig. 21 AFDD 50k60 contours of Mach number, advancing blade design point.

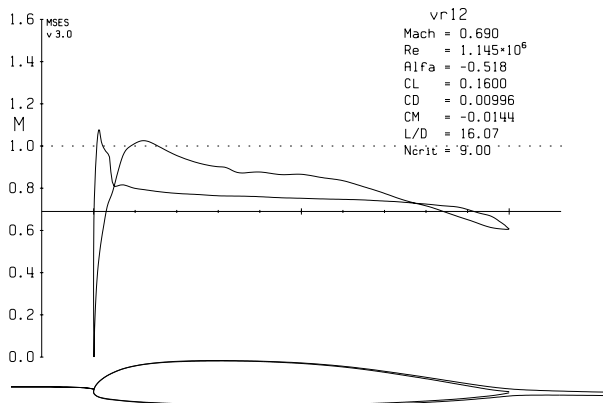


Fig. 20 Boeing VR12 airfoil results for advancing blade design point.

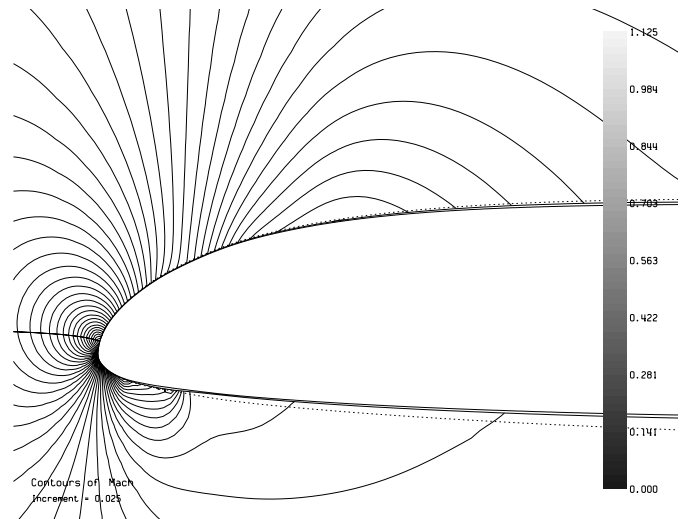


Fig. 22 VR12 contours of Mach number, advancing blade design point.

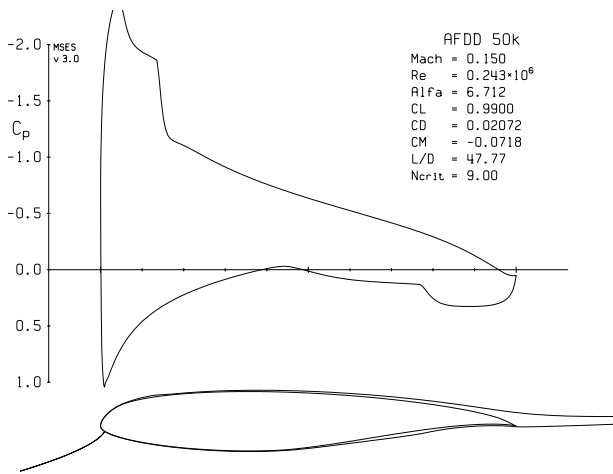


Fig. 23 Design results for retreating blade $r/R = 0.6$ before optimizer.

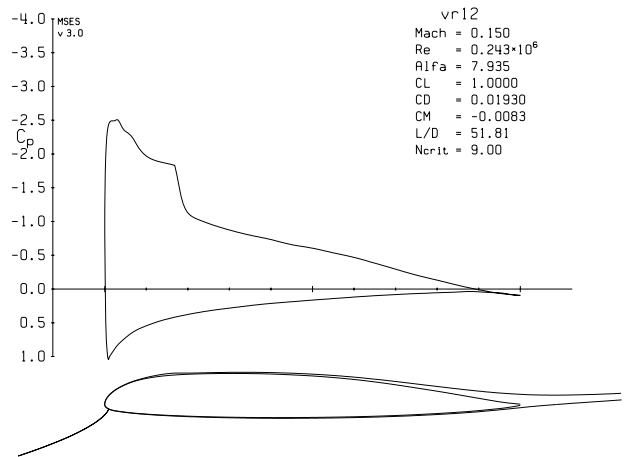


Fig. 25 Boeing VR12 airfoil results for retreating blade design point.

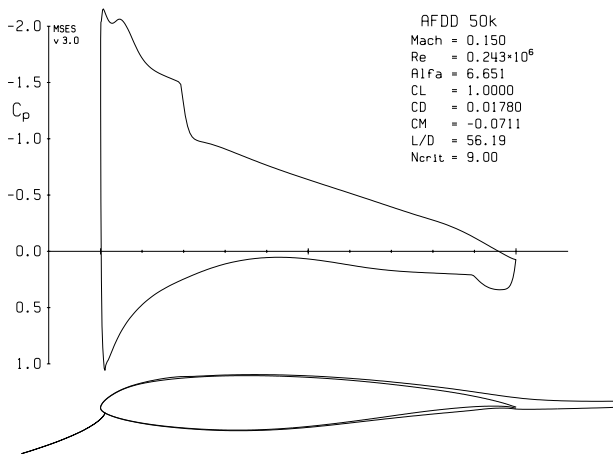


Fig. 24 AFDD 50k60 airfoil results for retreating blade design point.

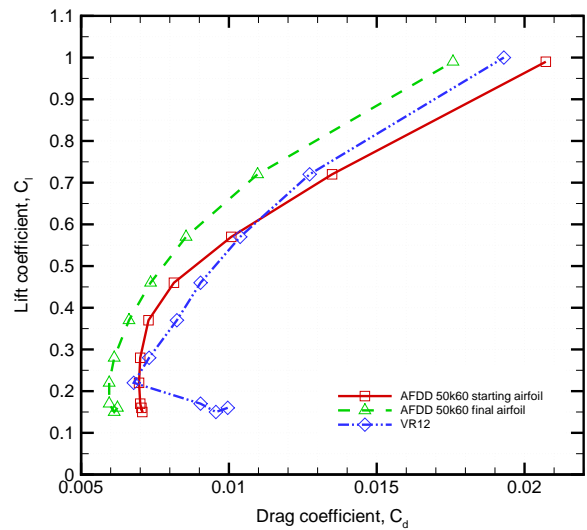


Fig. 26 Drag polar of the AFDD 50k60 airfoil before and after optimizer compared to VR12.

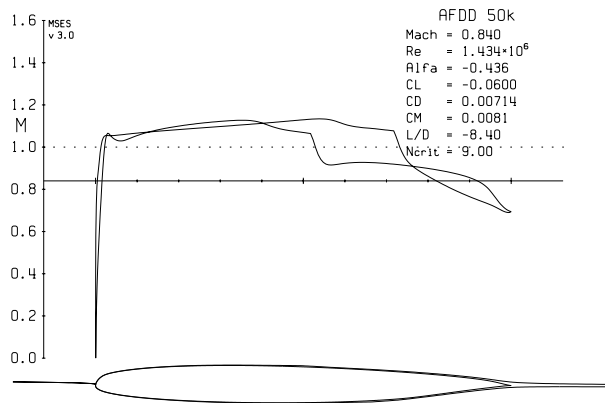


Fig. 27 AFDD 50k80 airfoil before optimizer, advancing blade design point.

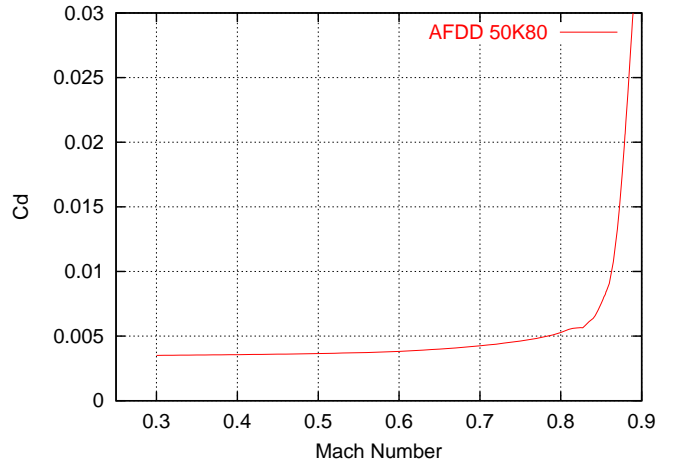


Fig. 29 AFDD 50k80 airfoil 70% natural laminar flow capability at zero lift.

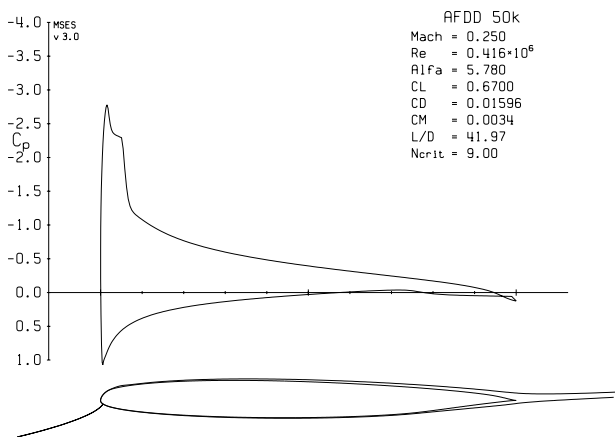


Fig. 28 AFDD 50k80 airfoil before optimizer, retreating blade design point.

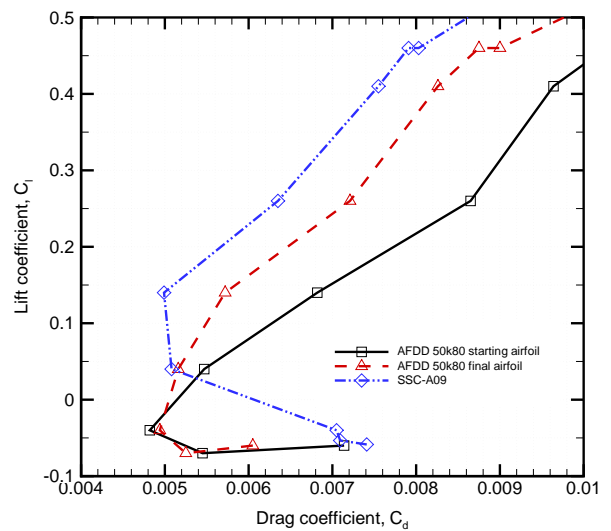


Fig. 30 Drag polar of the AFDD 50k80 airfoil before and after optimizer compared to SSC-A09.

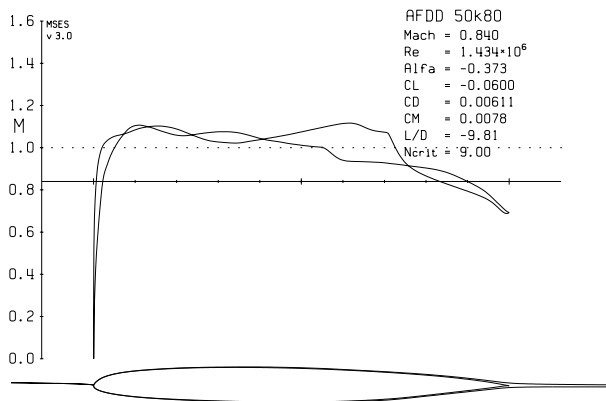


Fig. 31 AFDD 50K80, advancing blade design point.

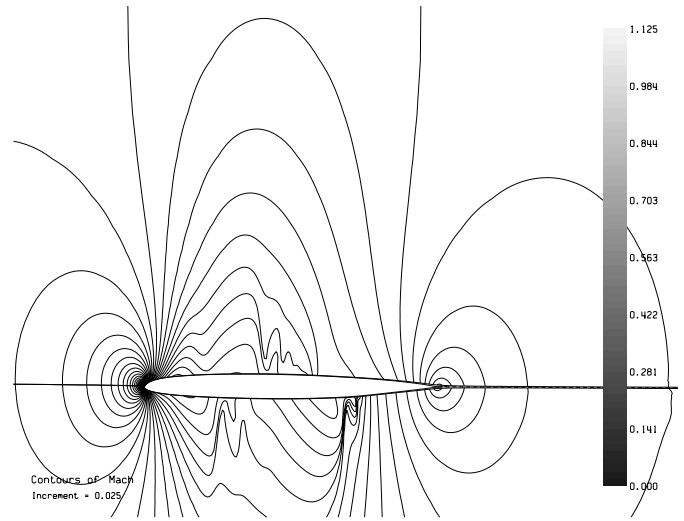


Fig. 33 AFDD 50k80 airfoil, contours of Mach number, advancing blade design point.

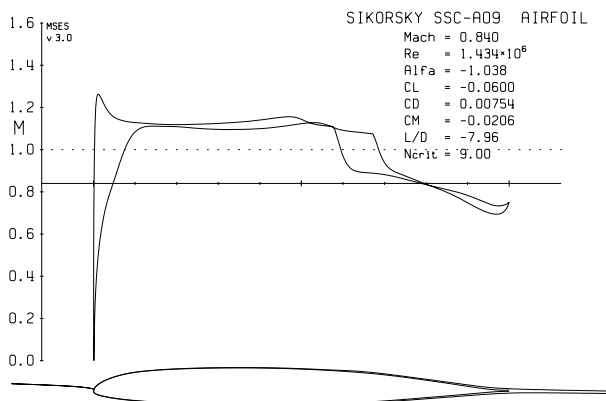


Fig. 32 Sikorsky SSC-A09 airfoil, advancing blade design point.

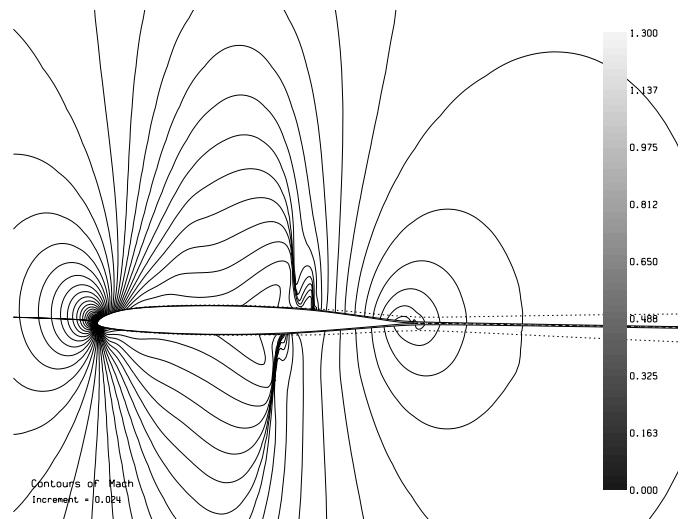


Fig. 34 Sikorsky SSC-A09 airfoil, contours of Mach number, advancing blade design point.